Boost multilevel cascade inverter for hydrogen fuel cell light railway vehicles

Krastev, Ivan; Tricoli, Pietro

Boost Multilevel Cascade Inverter for Hydrogen Fuel Cell Light Railway Vehicles

Ivan Krastev and Pietro Tricoli, *Member, IEEE*

***Abstract*— This paper presents a ground breaking traction drive for fuel cell-powered light rail vehicles based on a multilevel cascade converter with H-bridge cells. The converter provides dc-ac power conversion with unique buck-boost capability to compensate for the variation of fuel cell terminal voltage with the load power. In comparison to a conventional boost inverter, based on the cascade connection of a boost dc-dc converter and a voltage source inverter, the proposed converter has the significant benefits of much smaller inductor size, lower dc side current ripple, and multilevel voltage waveforms at the ac output. This paper presents the converter modelling and design of the boost inductor and sub-module capacitors, taking into account the full speed range of the motor. The concept has been fully validated on a bespoke experimental prototype driving an induction motor, showing the suitability of the proposed converter as a traction drive for hydrogen-powered rail vehicles.**

***Index Terms*— Fuel cell vehicles, modular multilevel converters, boost converters, traction drives.**

I. Introduction

RAILWAY electrification provides fast and reliable train journeys but requires large investments for the railway infrastructure. Therefore, many branch lines with moderate traffic will not be electrified over the next few decades and, hence, a fleet of diesel trains will be required to reach the destinations served by these lines, with raising concerns about journey times, pollution and noise. Hydrogen is an environmentally friendly alternative to diesel and could be used by a fuel cell to produce electrical power for the trains, achieving similar performance to their electric counterparts. At the present state of the art, independently powered electric and hybrid vehicles utilise a boost-type power converter to compensate for the variations of terminal voltage of the on-board power source [1],[2]. For hydrogen fuel cells, the considerable output impedance can result in voltage drop of 30-40% from no load to full load and compensation is normally required [3]-[5]. The power converter used to boost the voltage of the dc source increases the volume and weight of the vehicle, negatively affecting trains acceleration, performance, and energy consumption.

The standard approach to regulate the dc-link voltage of a voltage-source inverter is to use a boost dc-dc converter, a topology called boost voltage-source inverter (BVSI), but this uses high-current switching devices rated for the full voltage of the dc-link [6]. Both blocking voltage and current capabilities increase device switching losses, which in turn increase the weight, volume and cost of the cooling system, the input inductor and dc-link capacitor [7]. Control techniques such as amplitude modulated PWM can be used to reduce the size of the dc-link capacitor, without increasing devices' switching frequency [8]. This solution requires a wide bandwidth voltage controller that is difficult to implement in high-power traction converters, for which the required closed-loop bandwidth is close to the device switching frequency [9].

The size of the converter can also be reduced by interleaving multiple boost converter legs [6], [10], [11], where different types of inductors can be used [12]. It has been shown in [12] that coupled inductors offer a substantial reduction in volume and weight due to the converter's multilevel output and increase in effective switching frequency across the equivalent leakage inductor. However, the scaling the coupled inductor for additional phases prevents any intrinsic redundancy, as all converter legs need to be operational to avoid saturation of the coupled inductors.

Current-source inverters are also suitable for traction applications [13] as they achieve an output voltage boost, require smaller capacitors, and have sinusoidal voltage output waveforms compared to voltage source converters. However, the reverse blocking devices have high saturation voltage and at least 4 more devices are required to achieve bidirectional power flow, resulting in higher conduction losses.

Bidirectional Z-source inverters, quasi-Z-source inverters, and their derivative converters achieve voltage boost and inversion within the same power stage [14]. The current-fed quasi-Z-source inverter is particularly interesting as it offers a reduction in the total capacitance and a very low harmonic distortion of the output waveforms [15]. Voltage boost is limited to a factor of 2 during motoring [16] and the converter exhibits very high non-linearity when input current is close to 0, making it difficult to control during coasting and power reversal. A common limitation for all Z-source inverters is the need to overrate the power switches [17], which outweigh any

Manuscript received 7th of January 7, 2021, 16th of July 2021.
Ivan Krastev is with Tokamak Energy Ltd, Milton Park, Oxfordshire, OX14 4SD, U.K. (e-mail: ivan.krastev@tokamakenergy.co.uk).
Pietro Tricoli is with the Department of Electronic, Electrical and Systems Engineering, University of Birmingham, Birmingham, B15 2TT, UK (e-mail: p.tricoli@bham.ac.uk).

reduction in size of the passive elements.

The multilevel cascade converter (MCC) consists of a series of half-bridge (HB) or full-bridge (FB) submodules with floating capacitors. The main benefits of MCCs are multilevel output waveforms with low harmonic distortion, reduced size of magnetics, low switching losses, and intrinsic redundancy in case of faults of any of the submodules [18]. The HB MMC has been already examined in-depth for motor drives, with several strategies available for operations from dc to the maximum machine frequency [19]-[21]. As the FB MCC's module can generate both positive and negative voltage, the ac output voltage is no longer limited to the dc bus bar voltage of the input supply [22]. This important property has not been explored for traction applications yet. In [22], FB modules are used to reduce the sub-module capacitor voltage ripple at low machine frequency but the voltage boosting capability is not explored. In [23] the FB submodules are only used for low-frequency operations. In [24] an MCC with semi full-bridge modules is presented and the converter can boost the input voltage, but the main focus is on submodule design and converter control of a 2-phase prototype that is capable of only sourcing power. Importantly, while it has been discussed the basic idea that a FB MCC can boost the input voltage, there is no description of the actual boost properties of a non-ideal converter, and no experimental data showing bidirectional power flow with electric motors, using a defined strategy to decide boost ratios.

This paper proposes to use the topology of a FB MCC as a boost multilevel cascade inverter (BMCI) in a traction drive of a hydrogen fuel cell vehicle. This new converter enables a reduction of the volume and weight in comparison with the state-of-the-art topology, based on a boost DC/DC converter in cascade with a voltage source inverter. This is particularly important for traction drives, where reduction of weight and volume is essential to improve train's performance and increase payload. When operated in boost mode, the BMCI's peak output voltage increases as the input voltage goes down, resulting in a lower number of submodules compared to a HB MCC. Standard control techniques are still applicable [25], and capacitor voltage ripple at low machine speeds is reduced compared to a HB converter [21]. The proposed converter uses phase-shifted carrier pulse-width modulation (PSC-PWM) and a proportional state of charge (SOC) equalisation technique of capacitors to avoid interference with other controllers. The paper focusses on induction drives because induction motors are the most widely motors used for railway traction. However, the converter can be used also for permanent magnet motors by adapting only the motor control, so the main outcomes of this research are still applicable.

The concept is validated by a converter prototype driving an induction motor coupled to a steel flywheel. To simulate a traction load and, hence, demonstrate operations in 4 quadrants, the converter is tested under acceleration and dynamic braking, dissipating the energy through a braking resistor. As the BMCI has already been shown to be capable of integrating energy storage [26], it would be also well suited for hybrid trains with hydrogen fuel cells and batteries. Other possible applications are interfacing a low-voltage battery pack to the traction motor, reducing the size and weight of the power inductors, or a traction drive for a train with a dc supply with capabilities of compensating for the voltage variations of the traction power supply.

II. Boost Modular Cascaded Inverters

The proposed BMCI, shown in Fig. 1, uses the same topology as the MCC family: a number of series connected FB sub-modules with a floating capacitor form a converter arm; two connected arms make a converter leg with the middle point of the two arms used as phase output; three parallel connected legs to have a three-phase output. The key difference is that the BMCI uses FB sub-modules that can produce an ac voltage with amplitude higher than that of the input dc voltage. The fuel cell power supply is connected across the dc-link and provides the voltage V_{dc}, assumed to be smooth. The converter sub-modules operate as variable voltage sources, while the arm inductors can be modelled as controlled current sources and, when they are connected to the load, they can boost the input dc voltage. This effect is particularly useful to compensate for the regulation of fuel cells when the load increases.

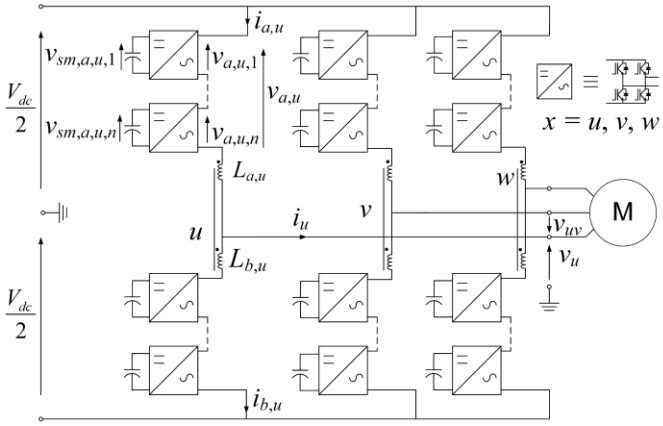

Fig. 1. Boost modular cascaded inverter schematic diagram.

III. Mathematical Model of the BMCI

As Fig. 1 shows, each arm is formed by n sub-modules that consist of 4 transistor switches and a capacitor, producing the arm voltages v_{xa} or v_{xb}, where x denotes the phase (u, v, or w), a denotes the arm connected to the positive input terminal, and b the arm connected to the negative input terminal. The arms voltages and current are given by the following equations:

$$\begin{cases} v_{x,a/b} = \dfrac{V_{dc}}{2} \mp v_x = d_{x,a/b} \displaystyle\sum_{i=1}^{n} v_{SMx,a/b,i} \\ i_{x,a/b} = i_{x,circ} \pm \dfrac{i_x}{2} \end{cases} \tag{1}$$

where $v_{x,a/b}$ can be either $v_{x,a}$ or $v_{x,b}$, $i_{x,a/b}$ can be either $i_{x,a}$ or $i_{x,b}$ and $i_{x,circ}$ is the circulating current between the dc source and the submodules, $v_x = V_{\max} \sin(\omega t)$ and $i_x = I_{\max} \sin(\omega t + \varphi)$ are the output voltage and current, supposed for simplicity sinusoidal at angular frequency ω, with amplitudes $V_{\max}$ and $I_{\max}$, respectively, and with the current shifted by an angle φ.

The top and bottom arm duty-cycles, $d_{x,a}$ and $d_{x,b}$, have two

components: a common duty-cycle that controls the circulating current between the dc source and the converter legs, $d_{x,circ}$; and a differential duty-cycle that controls the power exchange between the converter legs and the traction motor, $d_{x,diff}$:

$$d_{x,a/b} = d_{x,circ} \mp d_{x,diff} \tag{2}$$

where $d_{x,a/b}$ can be either $d_{x,a}$ or $d_{x,b}$. The values of the duty-cycles must satisfy the condition that $d_{x,circ} + d_{x,diff} \leq 1$ to ensure linear modulation. The differential duty-cycle can be represented as a function of the common duty-cycle and the modulation index for the output voltage, M:

$$d_{x,diff} = M\left(1-d_{x,circ}\right)\sin\left(\omega t-\theta_x\right) \tag{3}$$

where θ_x is 0, $-2\pi/3$, and $2\pi/3$ for x = u, v, w, and again it should be $M \leq 1$ to avoid overmodulation.

As in a buck-boost converter, the maximum voltage boost ratio is limited by the parasitic resistances of the circuit. For each BMCI arm, these are the parasitic resistances in the arm inductance r_L, the semiconductor devices r_{Si}, and the submodule capacitor r_C. Looking at an individual sub-module, two semiconductor devices are always conducting while the capacitor current is switched, so the total resistance is $2r_{Si}$. Also, it can be assumed that the difference between submodule capacitor voltages are small, so $v_{Cx.a/b,i} \approx v_C$ and $v_{SMx.a/b,i} \approx v_{SM}$ for $i = 1,2,\ldots, n$. With these considerations, the total inserted arm voltage and the submodule capacitor voltage are, respectively:

$$\begin{cases} v_{x,a/b} = d_{x,a/b}\; n\, v_{SM} + 2\, i_{x,a/b}\; n\, r_{Si} \\ v_{SM} = v_C + d_{x,a/b}\; i_{x,a/b}\; r_C \end{cases} \tag{4}$$

Combining (4) with (2) and (3), the inserted arm voltage becomes:

$$v_{x,a/b} = d_{x,a/b}\; n\, v_C + n\, i_{x,a/b}\left(2r_{Si} + d_{x,a/b}^2\; r_C\right) \tag{5}$$

According to (5), the equivalent series resistance of each sub-module consists of two components: a constant part that is the semiconductor switches' equivalent series resistance; and the capacitor resistance seen on the ac side of the module, which is variable with the duty-cycle and the average value over one cycle of the output waveform. The duty cycles $d_{x,a/b}$ can be approximated by their average quadratic values over one switching period, which are equal and, according to (2), can be written as:

$$d_{x,a/b} \cong d_{x,a/b,rms} = \sqrt{d_{x,circ}^2 + \frac{d_{x,diff}^{\;2}}{2}} \tag{6}$$

where $d_{x,a/b,rms}$ is the rms value of $d_{x,a/b}$. Substituting (6) into (5), the equivalent sub-module resistance r_{SM} is:

$$r_{SM} \cong 2\, r_{Si} + \left[d_{x,circ}^2 + \frac{d_{x,diff}^{\;2}}{2}\right] r_C \tag{7}$$

The equivalent circuits representing the BMCI with the parasitic elements are shown in Fig. 2, where C is the sub-module capacitance, L is the leg equivalent inductance, R_x is the phase load resistance and L_x is the phase load inductance. For simplicity of derivations, a R-L static load has been used for the calculations, but the validity of the results is not affected as the mechanical time constant of the motor is significantly slower

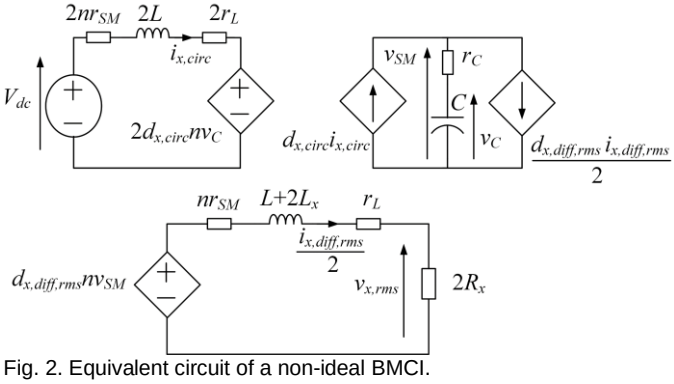

Fig. 2. Equivalent circuit of a non-ideal BMCI.

than the electrical time constants of the converter. The average values of the ac-side duty cycles and currents will be zero and, to get a representative result, the output current $i_{x,diff}$ and the differential duty cycle $d_{x,diff}$ are replaced by their rms values, $i_{x,diff,\mathrm{rms}}$ and $d_{x,diff,\mathrm{rms}}$, respectively.

If there is no saturation of the arm duty-cycle, the control variables M and $d_{x,circ}$ are independent and so the current $i_{x,diff,\mathrm{rms}}$ can be calculated from the circuit at the bottom of Fig. 2 and substituted in the circuit at the right of Fig. 2 for a more straightforward controller design. The rms output current and equivalent sub-module load resistance are:

$$i_{x,diff,rms} = \frac{\sqrt{2}(1-d_{x,circ})M\; n\, v_{SM}}{\sqrt{\left(2R_x + r_L + n\, r_{SM}\right)^2 + \left[\omega\left(L+2L_x\right)\right]^2}} \tag{8}$$

$$R_{x,SM} = \sqrt{2}\,\frac{\sqrt{\left(2R_x + r_L + n\, r_{SM}\right)^2 + \left[\omega\left(L+2L_x\right)\right]^2}}{\left[\left(1-d_{x,circ}\right)M\right]^2 n} \tag{9}$$

Assuming also that $v_{SM} \approx v_C$, the converter circulating current and sub-module voltage are defined by the following equations:

$$\begin{cases} \dfrac{di_{x,circ}}{dt} = -\dfrac{(r_L + r_{SM})}{L} i_{x,circ} - \dfrac{d_{x,circ} n\, v_C}{L} + \dfrac{1}{L}\dfrac{V_{dc}}{2} \\ \dfrac{dv_C}{dt} = \dfrac{R_{x,SM}}{C\left(R_{x,SM} + r_C\right)} d_{x,circ} i_{x,circ} - \dfrac{1}{C\left(R_{x,SM} + r_C\right)} v_C \end{cases} \tag{10}$$

The average state-space model can be used to derive the large signal boost ratio of the converter by setting all derivatives to 0, solving for $v_C \approx V_C$, and considering that the rms ac component of the arm voltage, $V_{x,\mathrm{rms}}$, is:

$$V_{x,rms} = \frac{M}{\sqrt{2}}\left(1-d_{x,circ}\right) n\, v_C \cong \frac{M}{\sqrt{2}}\left(1-d_{x,circ}\right) n\, V_C \tag{11}$$

Therefore, the steady-state voltage boost ratio is:

$$G_V = \frac{V_{x,rms}}{V_{dc}} = \frac{M}{2\sqrt{2}}\,\frac{n\, R_{x,SM}\; d_{x,circ}\left(1-d_{x,circ}\right)}{n\, R_{x,SM}\; d_{x,circ}^2 + r_L + r_{SM}} \tag{12}$$

Equation (12) highlights that the voltage boost ratio characteristic of the BMCI is similar to that of a buck-boost converter in cascade to a voltage-source inverter. Also, the BMCI uses two variables, $d_{x,circ}$ and M, to control the output current and the voltage of submodule capacitors, respectively.

To understand how the BMCI achieves buck-boost operations, it is possible to refer to the circuit in Fig. 3. For simplicity, only phase u and 2-submodule per arm are considered during one half-cycle of the output waveform i.e.,

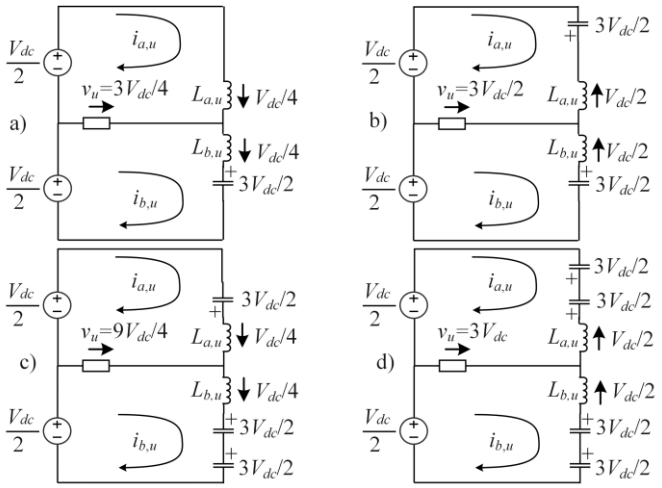

Fig. 3. Equivalent circuits for boost mode when n = 2: a) and c) inductors discharging, b) and d) inductors charging.

$v_u > 0$. In circuits (a) and (b), the two switching states at $d_{circ} = 1/6$ and $d_{diff} = 1/3$ are shown. The phase voltage v_u switches between $3V_{dc}/4$ and $3V_{dc}/2$, with an average value during the PWM cycle equal to $V_{dc}/2$, and hence buck operations. In circuits (c) and (d), the two switching states at $d_{circ} = 1/6$ and $d_{diff} = 5/6$ are shown. In this case, the phase voltage v_u switches between $9V_{dc}/4$ and $3V_{dc}$, with an average value during the PWM cycle equal to $5Vdc/2$, boosting the output voltage. In each of the two cases of d_{diff}, the average voltage across the inductors is equal to 0 over the PWM cycle by modulating appropriately between circuits (a) and (b) and (c) and (d).

IV. Design of the BMCI for a Fuel Cell Rail Vehicle

This section describes the design of the proposed BMCI for a light rail vehicle powered by a hydrogen proton exchange membrane (PEM) fuel cell. The light railway vehicle, formed by 7 cars and powered by 12 induction motors fed in pairs by 6 traction converters, has a typical urban use and its main data are shown in Table I. The PEM fuel cells internal parameters have been determined using the methodology in [27]. Each traction inverter is supplied by 2 fuel cells, arranged with 2 stacks in parallel. As the motor voltage is boosted by the BMCI, this avoids the series connection of fuel cells and improves the redundancy of the traction power supply in case of a fuel cell fault. In the standard electrical configuration, the traction power supply operates at 750 V dc that equates to a nominal motor voltage of 450 V rms with 3rd harmonic injection. In the proposed configuration with PEM fuel cells, the operating voltage of the motor remains approximately the same to guarantee the same performance.

The design of the BMCI for this light rail vehicle requires the definition of the number of submodules per arm, the semiconductor devices, the submodule capacitance and the arm's inductance. The model of previous section can be used to design accurately these quantities. Specifically, the analytical linearised model allows the determination of the required sub-module capacitance, while the time variant model enables the determination of the required leg inductance. The inductor design takes into account the variable value of the common duty-cycle $d_{x,circ}$ and phase shift between the modulation carrier groups of arms *a* and *b*.

TABLE I.
MAIN DATA OF THE LIGHT RAIL VEHICLE UNDER STUDY

Mass, loaded	80 tonnes
Maximum speed	70 km/h
DC-link voltage	750 V
Maximum tractive effort	100 kN
Traction motor power	80 kW
Nominal motor voltage	450 V rms
Nominal motor current	130 A rms
Nominal power factor	0.85
Stator and rotor resistances	0.07 Ω and 0.059 Ω
Stator and rotor inductances	203μH and 203 μH
Magnetising inductance	6.2 mH
Base frequency	100 Hz
Base speed	1945 rpm
Fuel cell rated power	93 kW
Fuel cell open circuit voltage	360 V
Fuel cell voltage at rated power	220 V
Fuel cell rated current	423 A
Fuel cell ohmic resistance	26 mΩ
Fuel cell activation resistance	246 mΩ
Fuel cell activation capacitance	4.6 mF

A. Choice of number of sub-modules

The number of submodules, n, depends on the required peak arm voltage and number of inverter output voltage levels. In a conventional MCC, the number of phase voltage levels is directly proportional to n, while in a FB MCC converter they have a higher value, as each sub-module produces 3 voltage levels. For a BMCI, the maximum available voltage levels is dependent on the circulating duty cycle $d_{x,circ}$, and lower values allow for higher utilisation of the modulation range.

B. Semiconductor devices

For BMCI, the worst-case arm current occurs at rated power, because when the motor draws the max ac current at standstill the input dc current is very small. Therefore, considering that there are 4 devices per sub-module and 6 arms, the total apparent power of the semiconductor devices is:

$$S_{sw,total} = 24 \times \sqrt{I_{dc,x}{}^2 + \left(\frac{I_{ac,x}}{2}\right)^2} \times n\left(V_C + \frac{\Delta v_C}{2}\right) \qquad (13)$$

where Δv_C is the designed voltage ripple across the sub-module capacitor, $I_{dc,x}$ and $I_{ac,x}$ are the average and alternating component of the current i_x.

C. Submodule capacitors

The energy stored in each arm depends only on the converter output voltage, the fundamental frequency and instantaneous power. The minimum capacitance to achieve a certain voltage ripple value can be calculated as:

$$C_{arm} \geq \frac{\Delta w_{x,a/b}}{\Delta v_{Cx,a/b}\, V_C} \qquad (14)$$

where $\Delta w_{x,a/b}$ is the peak energy fluctuation and $\Delta v_{Cx,a/b}$ is the voltage ripple. Equation (14) has been obtained assuming that the capacitor voltage ripple is symmetrical around the nominal operating point, V_C. Also, $\Delta w_{x,a/b}$ can be calculated from the instantaneous arm's power $p_{x,a/b}$:

$$\Delta w_{x,a/b} = \max\left(\int_0^T p_{x,a/b}(t)dt\right) - \min\left(\int_0^T p_{x,a/b}(t)dt\right) \quad (15)$$

where the instantaneous power arm is:

$$p_{x,a/b} = \pm\frac{n\,V_C\;d_{x,circ}I_{\max}}{2}\sin\left(\omega t+\varphi\right)\mp M^2\frac{\left(1-d_{x,circ}\right)^2}{4\,d_{x,circ}}\times \quad (16)$$
$$\times n\,V_C I_{\max}\sin\left(\omega t\right)+\frac{M\left(1-d_{x,circ}\right)}{4}n\,V_C I_{\max}\cos\left(2\omega t+\varphi\right)$$

For a traction converter, the submodule capacitance should then be designed according to the peak energy fluctuation over the full speed range of the converter, including field weakening, where the converter is operating at constant output power. This can be achieved by increasing the output frequency, output power, and voltage boost ratio up to base speed (constant torque region), and then keeping constant the power and voltage boost ratio, while increasing frequency (constant power region).

The capacitor energy fluctuation over frequency and phase angle of the current φ can be plotted to find the peak energy storage demand, as Fig. 4 shows for the vehicle under study and various voltage boost ratios G_V. All the curves have the same projection on the plane "frequency, phi", as also illustrated in Fig. 4. This is because for each value of the fundamental frequency the phase angle of the current is constant in the constant torque region, as the direct and quadrature components of the motor current are constant; and then increases in the field weakening region as the reactance increases.

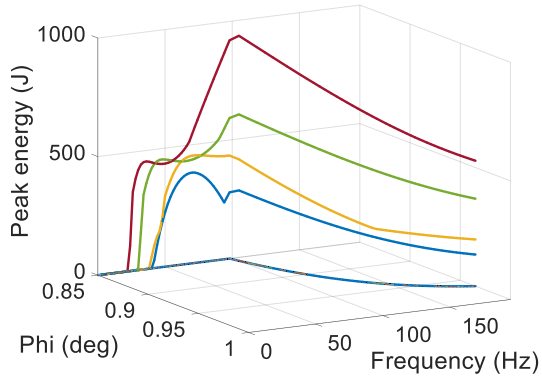

Fig. 4. Capacitor energy fluctuation demand for G_V = 1 (blue), G_V = 2 (yellow), G_V = 3 (green), G_V = 4 (red) as a function of the machine fundamental frequency and phase angle of the current.

For higher G_V values, the peak energy requirement increases; for voltage boost ratios greater than 2, the peak value occurs at the rated frequency, which is 100 Hz for the simulated vehicle. In practice, due to the second harmonic in the arm energy fluctuation, the nominal capacitor will be in the range defined by (14), but with an error from the desired average voltage, V_C. This error has been shown to be small during motoring operation, with current displacement angle between 0 and π/2 [28]. Thus, the method presented in this paper is valid for the design of the capacitance, whereas an in-depth investigation of the exact voltage ripple can be made according to the methodology presented in [28].

D. Leg inductors

The inductor design value is that of the total leg inductance L_{leg}=2L. The inductance value must be sufficiently large to meet the maximum inductor current ripple requirement. The current ripple of interest is that of the circulating current, as it flows through the input source, which can be sensitive in case of a hydrogen fuel cell.

Each arm produces a voltage $v_{x,a}$ and $v_{x,b}$ and they comprise of a dc offset, an ac component proportional to the modulation signal $d_{x,diff}$, and a switching component at the arm switching frequency, which is equal to 2n times the individual transistor switching rate f_{sw}. The pulse width and shape of the resultant inductor voltage varies as $d_{x,diff}$ is modulated, passing through 3 possible boundary conditions: pulse doubling, pulse coincidence, and single pulsation.

Pulse doubling occurs when the mid-point of the pulse of one arm is aligned with the middle of a pulse with the opposite polarity from the other arm. The resultant waveform has a voltage step of V_C, and oscillates at frequency of 4 n f_{sw}. Pulse coincidence occurs when the two converter arms have equal duty-cycles that are also aligned, creating a pulse with a voltage step of 2V_C and frequency of 2 n f_{sw}. Single pulsation occurs when one arm's duty cycle is at a boundary between two converter levels, and the resultant arm voltage is a constant value. In this situation the voltage $v_{L,circ}$ is solely dependent on arm that is switching, with a resultant voltage step V_C and frequency 2 n f_{sw}. The highest current ripple will occur for the pulse coincidence case, as the voltage step is twice high as the other cases, and the switching frequency is smaller than the pulse doubling case. The value of the duty cycle for which there is pulse coincidence, d_{coinc}, is dependent on the time shift between the carrier groups of arms a and b, t_{shift}, and can be calculated by the following equations:

$$d_{coinc} = \begin{cases} nd_{x,circ} - \text{floor}\left(nd_{x,circ}\right),\ t_{shift}=0 \\ nd_{x,circ} - \text{round}\left(nd_{x,circ}\right)+0.5,\ t_{shift}=\dfrac{1}{4nf_{sw}}, d_{x,circ} > \dfrac{1}{2n} \\ \dfrac{d_{x,circ}+0.5}{n},\ t_{shift}=\dfrac{1}{4nf_{sw}},\ d_{x,circ} < \dfrac{1}{2n} \end{cases} \quad (17)$$

The required total leg inductance can be derived using (17) and the predefined peak current ripple $\Delta i_{x,circ,\max}$:

$$L_{leg} \cong \frac{1}{\Delta i_{x,circ,\max}} d_{coinc}\left(1-d_{coinc}\right)\frac{V_{dc}}{2n^2 f_{sw}} \quad (18)$$

Equation (18) highlights that the leg inductance quadratically reduces with the number of submodules for $n \geq 2$ that demonstrates the advantage in the reduction of required boost inductance of the BMCI.

E. Design of the BMCI and comparison with a standard dual-stage boost inverter

For the calculation of the BMCI parameters, it has been assumed that motor voltage is the same as the standard light electric vehicle, i.e. 450 V rms phase-to-phase. Combining (11) and (12) we have:

$$V_{x,rms} = \frac{1}{\sqrt{2}}\left(MnV_c - \frac{V_{dc}}{2}\right) < \frac{1}{\sqrt{2}}\left(nV_c - \frac{V_{dc}}{2}\right) \quad (19)$$

Considering that the nominal fuel cell voltage is 220 V, that

means G_V = 1.2 and a total dc arm voltage of 600 V would be sufficient to keep M < 1. Therefore, with n = 1 the blocking voltage of semiconductor devices is 20% lower than the standard converter and so are switching losses. To take advantage of the reduction of the leg inductance, it has been chosen n = 2, that means that a smaller blocking voltage is required, e.g. 600 V instead of 1,700 V typical of standard converters. However, this has to be traded off with the higher number of semiconductor devices used in the converter, i.e. 48 instead of 4+6 of a standard BVSI, composed by a boost dc-dc converter with interleave and a 2-level voltage source inverter. Using the design methodology explained in this section and assuming Δv_C =60 V, or 20% of the nominal voltage, similar to values used in other works [19], [22], the main parameters of the BMCI are reported in Table II.

TABLE II
DESIGN PARAMETERS OF THE BMCI FOR THE LIGHT RAIL VEHICLE

Sub-module dc voltage	300 V
Sub-modules per arm	2
Total number of switches	48
IGBT switching frequency	4 kHz
Sub-module capacitance	2.35mF
Leg/phase dc current	250 A
Leg inductance	62µH
Leg coupling factor	0.9
Leg inductor parasitic resistance	4mΩ

In order to evaluate the effectiveness of the BMCI as a traction converter, the energy stored by passive elements and associated weights and volumes have been compared with a BVSI, as shown in Table III. The basis for comparison is the same output and input currents, the same input (fuel cell) and output (motor) voltages and current.

TABLE III
COMPARISON BETWEEN A BMCI AND A BVSI

Parameter	BMCI	BVSI
Semiconductor apparent power	4.6 MVA	2.6 MVA
Capacitor energy	5.4 kJ	0.4 kJ
Capacitor volume	27 dm^3	1 dm^3
Capacitor mass	28 kg	1 kg
Inductor energy	7.0 J	43 J
Inductor volume	18 dm^3	54 dm^3
Inductor weight	42 kg	259 kg
Energy storage volume	48 dm^3	55 dm^3
Energy storage mass	49 kg	260 kg
Efficiency at full load	93%	97%
Weighted THD	20%	60%

The BMCI's inductor is much smaller than the BVSI one, and even though the required capacitance is much larger, the BMCI system total energy storage components are smaller and considerably lighter, fulfilling one of the most stringent requirement of traction systems. The main drawback of the BMCI is its lower efficiency at full load, resulting in a larger cooling system that would partly reduce the gains of smaller energy storage components. However, it has to be pointed out that the power losses of the BMCI are mainly conduction losses and, as such, decrease almost quadratically with the load as for induction motors the magnetizing current is in the range of 20% of the nominal value. Therefore, the efficiency curve of the BMCI is expected to be quite flat at light loads, whereas the same curve of BVSI is expected to decrease more quickly, as the majority of losses are switching losses and hence, independent on the load.

For traction applications, where the load is continuously changing, the average efficiency is more important than the peak efficiency and hence, a more detailed study on typical traction cycles would be needed to compare the total energy losses of the two converter topologies. Additionally, the weighted harmonic distortion of the BMCI is much smaller even if the capacitor ripple is higher, reducing motor losses and associated requirements of cooling systems. This is because the capacitor's ripple has only a modest effect on the harmonic distortion in comparison to the switching frequency and the multilevel waveform. It is estimated that the reduction of motor losses would bring the BMCI almost on par with the BVSI, depending on the specific motor and level of field weakening, where the higher current distortion has a significant impact.

V. CONTROL OF BMCI

Fig. 5 show the control system of the proposed BMCI. The control of the motor is based on vector control and produces the duty-cycle $d_{x,diff}$, as indicated at the center of Fig. 5. The reference quadrature current, i_{q*}, is generated by a closed-loop speed controller comparing the actual rotating speed ω_r with the reference ω_{r*}. The reference direct current, i_{d*}, is generated by a flux regulator, where $\Phi_{r,d}$ is the total rotor flux, estimated by the actual current i_d and the rotor time constant, τ_r. The actual i_d and i_q components of the ac current, $i_{ac,x}$, are calculated from the rotor flux position ψ_{ac}, which is estimated using a standard indirect method based on the slip frequency ω_{slip} and rotor electrical velocity equal to $p\omega_r$, being p the number of pole pairs. The stator frequency, ω_{ac}, is used in the decoupling block of i_d and i_q through the constant factor K_{iac}. The current regulators provide finally the values of $d_{x,diff}$.

The duty-cycle $d_{x,circ}$ is generated by a regulator on the current component $i_{x,circ}$, as shown at the top of Fig. 5. The reference $i_{x,circ}$* is obtained by a voltage controller on the average value of the total dc arm voltage, $\overline{v}_{x,dc}$, compared to the reference $V_{dc}/2$. To balance the voltages between arms in the same leg, an additional proportional feedback loop injects a balancing current $i_{x,bal}$*. The output of the arm balancing compensator is modulated by a signal y', which is a term either oscillating at the ac-side frequency or a square-wave in phase with d_{comm} to enable power transfer between the two arms of the same leg, as explained in the following paragraph.

When the ac-side frequency is below a critical value ω_{min}, depending on the specific converter ratings and parameters, the power oscillations in the sub-module energy storage become unmanageable, as described extensively in [19], [21]. To avoid this effect a low-frequency compensation mode is enabled. This mode injects a compensating power by adding a duty-cycle d_{comm} oscillating at angular frequency $\omega_{comm} > \omega_{min}$ that is differential to arm a and b in a converter arm, but common to all legs:

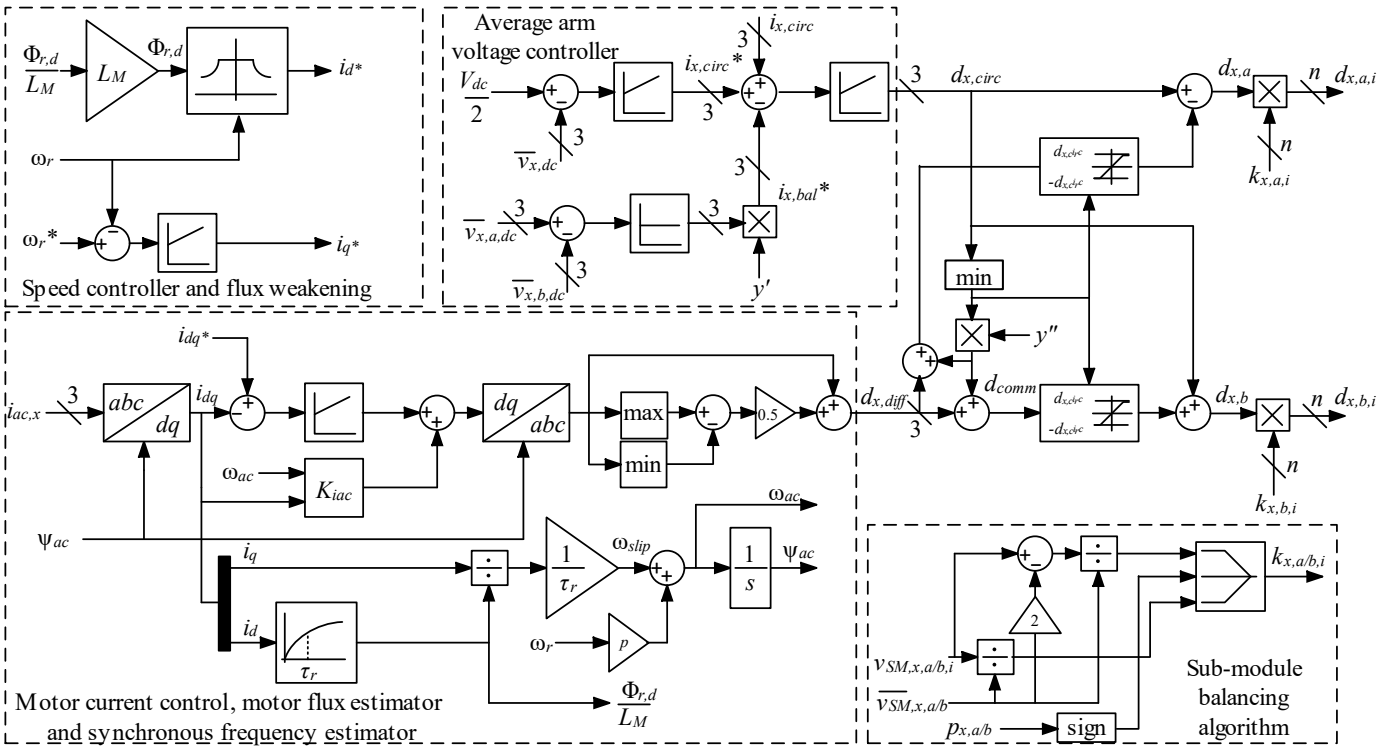

Fig. 5. Block diagram of the control of the BMCI for fuel cell rail vehicles

$$d_{x,a/b} = d_{x,circ} \mp \left(d_{x,diff} + d_{comm} \right) \tag{20}$$

To avoid saturation of any of the arm duty-cycles, d_{comm} is calculated using the smallest of the 3 $d_{x,circ}$ duty-cycles:

$$d_{comm} = y'' \times \min\left(d_{x,circ} \right)\Big|_{x=u,v,w} \tag{21}$$

where:

$$y'' = \begin{cases} sign\left(\sin \omega_{comm} t\right) & \omega_{ac} < \omega_{\min} \\ 0 & \omega_{ac} > \omega_{\min} \end{cases} \tag{22}$$

Finally, at the bottom right of Fig. 5 it is shown the individual balancing of sub-module capacitors. If the individual voltages $v_{SM,x,a/b,i}$ are higher than the average value of the arm, $\overline{v}_{SM,x,a/b}$, the duty-cycles $d_{x,a/b}$ will be modified by a factor $k_{x,a/b,i}$ equal to $v_{SM,x,a/b,i} / \overline{v}_{SM,x,a/b}$ that amplifies $d_{x,a/b}$ if the arm power $p_{x,a/b}$ is positive (from the sub-module capacitors to the ac output) and attenuates it if it is negative.

VI. Simulation Results

A simulation study has been undertaken to assess the performance of the proposed BMCI for a fuel cell light train with a typical traction cycle consisting of acceleration, coasting and braking up to a stop. The most important variables of the motor and the converter are presented in Fig. 6.

As predicted from the model, the converter operates as a buck inverter, i.e. boost ratio lower than 1, up to the speed of approximately 18 km/h and then as a boost inverter up to the maximum speed of 70 km/h. The boost ratio compensates also for the fuel cell voltage drop, as it can be seen by the variation of $d_{u,circ}$ that changes from 0.24 (no load) to 0.19 (full load). The same figure also shows that $d_{u,diff}$ has fundamental frequency related to the motor speed and torque, and that $d_{u,circ} + |d_{u,diff}|$ is maintained below 1 to avoid overmodulation.

For the initial part of the acceleration at constant torque, both the components *d* and *q* of motor current are constant, as both are controlled to regulate torque and rotor flux linkage to a constant value. The *d* current component reduces when the motor enters field weakening to allow for constant motor voltage. The diagram of the input current shows the two different zones of constant torque from 1 to 25 seconds and constant power from 25 to 32 seconds. After 32 seconds, the speed reaches the reference value and the current i_q has a much smaller value, as expected with an inertial load like a train.

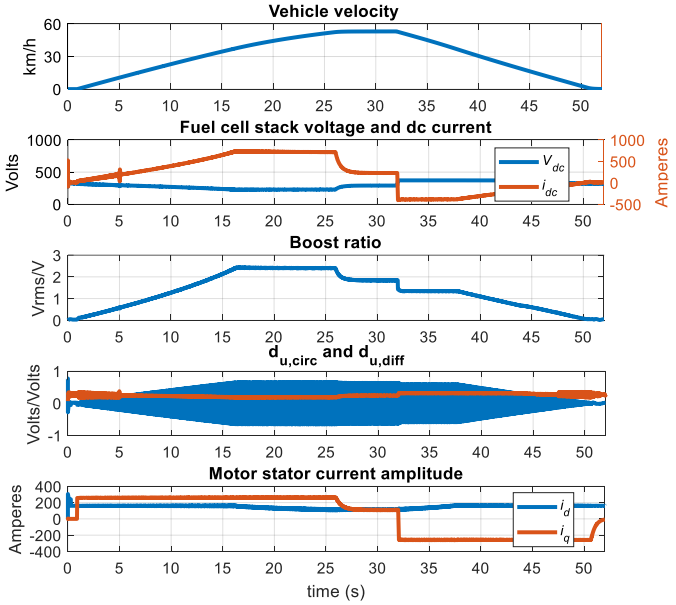

Fig. 6. Simulation of BMCI performance for a traction cycle.

VII. Experimental Validation

The operations of the proposed converter have been experimentally validated using the laboratory prototype shown in Fig. 7 and whose main data are reported in Table IV. A DC power supply has been used to simulate the fuel cell due to restriction in the use of hydrogen in the lab.

As the prototype BMCI cannot produce the motor's nameplate voltage levels, the base frequency, after which the machine is operated in field weakening, has been lowered to 20 Hz, and the ratio of i_q and i_d has been adjusted accordingly.

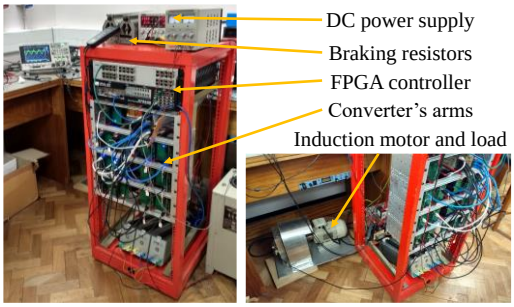

Fig. 7. BMCI hardware prototype setup.

TABLE IV
PARAMETERS OF THE EXPERIMENTAL CONVERTER

Number of modules per arm	n	2
Submodule capacitance	C	2.2 mF
Capacitor parasitic resistance	r_C	55 mΩ
Leg inductance	L_{leg}	1.3 mH
Inductor series resistance	r_L	34 mΩ
IGBT collector-emitter resistance	r_{CE}	25 mΩ
Nominal DC-link capacitor voltage	V_C	75 V
Maximum capacitor ripple	Δv_C	7.5 V
Input voltage	V_{dc}	48-60 V
Input current	I_{dc}	8.7 A
Peak line-to-line motor voltage	$V_{LL,\max}$	200 V
Motor base speed	n_b	750 rpm
Peak motor current	$I_{\max}$	3.5 A
Voltage boost ratio	$G_{V,rms}$	2.83

The first test has been carried out with a static ohmic-inductive load to verify the maximum boost ratio, using open-loop control for the circulating duty-cycle d_{circ}, while the amplitude of the differential duty cycle d_{diff} has been maintained at $(1 - d_{circ})$. The measured boost characteristics are shown in Fig. 8 and compared to the results of the model developed in section III. The figure shows a very good agreement between

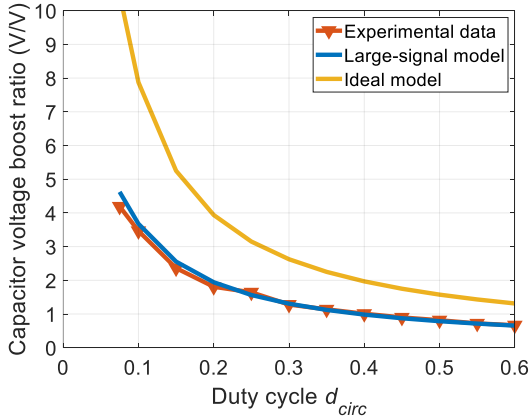

Fig. 8. Voltage boost ratio comparison between an ideal BMCI, analytical model, and experimental prototype.

the analytical model and the experimental results. As expected, the ideal voltage boost ratio of the BMCI is higher than that of the prototype converter due to the parasitic elements. This result points out the importance of the accurate modelling carried out in section III to estimate the voltage boost ratio, especially when either a high number of submodules is used or the parasitic elements cannot be neglected.

A second experiment has been carried out to verify the transient response of the converter, as shown in Fig. 9, for a step variation of the capacitor voltage from 40 V to 60 V. During this test, the modulating index has been kept constant, so the voltage variation causes an increase on the input and phase current as the load impedance is constant. The experiment shows that the arm's voltage controller can successfully balance the capacitor voltage during the transient with a transient time of approximately 100 ms.

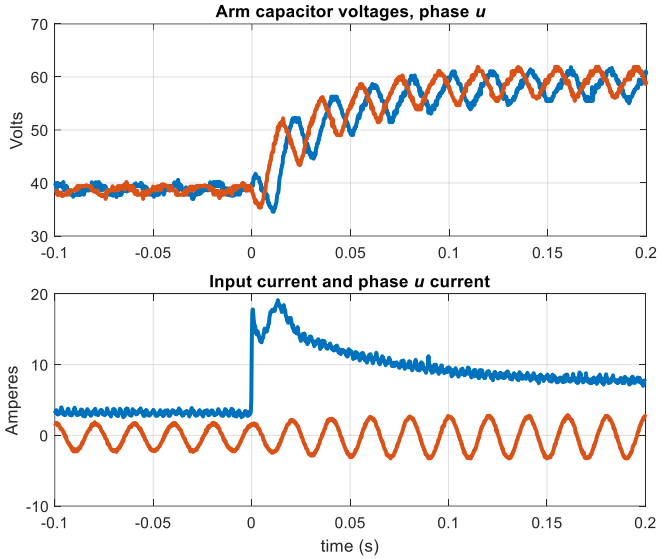

Fig. 9. Step response of capacitor voltage reference.

A third experiment has been carried out with the induction motor for the same traction cycle of the simulated model, albeit scaled for the prototype. The most important variables of the converter are presented in Fig. 10. The converter provides low voltage at low speed and, hence, operates as a buck inverter. When the speed increases and reaches the constant power speed range, the converter operates instead as a boost inverter. For the initial part of the acceleration, both the motor d and q currents are constant, as both components are controlled to set the desired values of torque and rotor flux linkage. The d current component reduces when the motor enters field weakening to allow for constant motor voltage. The diagram of the input current shows the two different zones of constant torque from 0 to 3 seconds and constant power from 3 to 6.5 seconds. After 8 seconds, the speed reaches the reference value and the current has a much smaller value, as expected with an inertial load. The voltage and current waveforms, not shown here for brevity, show the reduced harmonic distortion typical of MMCs.

As for any MCC, the proposed BMCI has critical operations at rated output current, low modulation index and low fundamental frequency, as there is a large voltage ripple across the submodule capacitors. This has been compensated by the

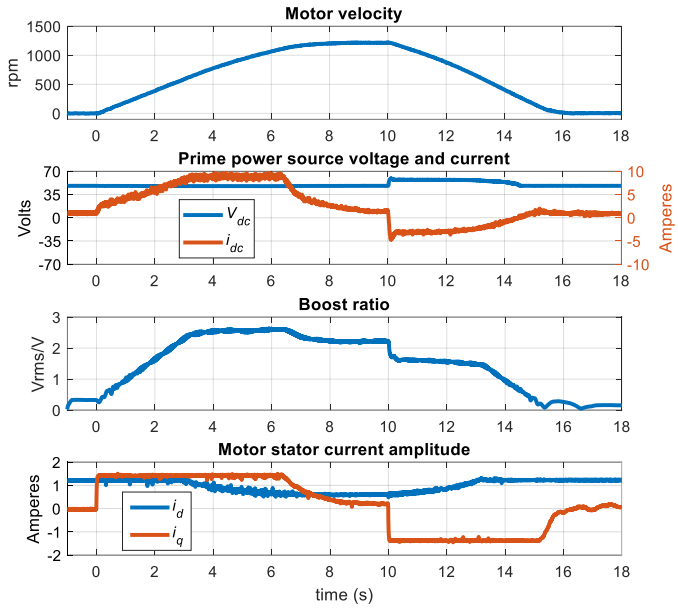

Fig. 10. Experimental results of the BMCI for a typical traction cycle.

control algorithm described at section V and can be closely examined in Fig. 11. It shows the sub-module capacitor voltages of two arms during the traction cycle of Fig. 10, as well as the respective arm currents. At start-up from 0 to 1.6 s, the voltage ripple is contained and the low-frequency compensation scheme is operating as expected. At t = 1.6 s, it can be seen that the converter returns to normal operations by the abrupt change of the arm current. The designed peak capacitor voltage ripple of 7.5 V is achieved exactly at the motor's base speed as predicted by the theoretical analysis. During regenerative braking operations, at t = 15 s, the low-frequency compensation is again engaged to limit the capacitor voltage ripple when the motor decelerates down to zero speed.

At higher frequencies the converter is supplying power to the electric motor and in the constant power region operates with a fixed boost ratio. Zoomed waveforms in this condition have been captured in Fig. 12. The converter operates with a high

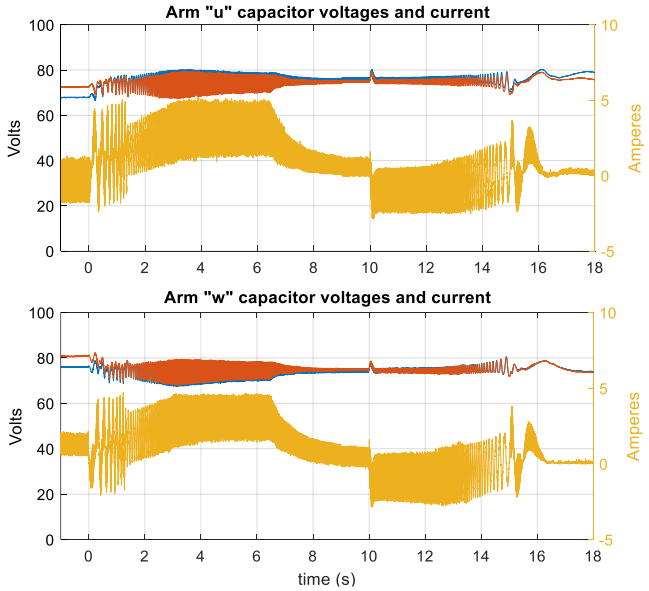

Fig. 11. Sub-module capacitor voltage (blue and red for each sub-module), and arm current (yellow) for the cycle of Fig. 10.

boost ratio, with the peak voltage being 4 times higher than the dc source. During braking, the BMCI must invert the motor i_q current and starts recovering part of the kinetic energy of the flywheel. This condition is shown in Fig. 13. The braking power is dissipated in a braking chopper connected to the dc terminals of the converter. Before and immediately after the start of braking, the converter operates with a voltage boost, but a lower factor than during acceleration as the voltage V_{dc} is above the no-load voltage of the fuel cell to activate the braking resistors.

Finally, Fig. 14 shows the voltage across the arm inductor with a carrier frequency of 6.25 kHz to demonstrate the effect of the chosen modulation. It can be seen that the effective switching frequency is 50 kHz and, hence, 4×n times the carrier frequency, demonstrating the effect on the reduction of ripple due to the multilevel waveform. The pulse coincidence events can also be seen when the voltage step is equal to 2×V_C. This occurs when the edges of the top and bottom arm switching

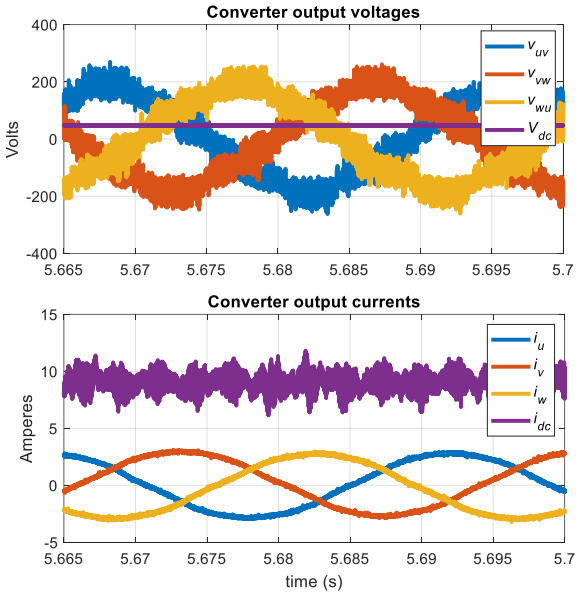

Fig. 12. Motoring operations of the prototype BMCI in boost conditions.

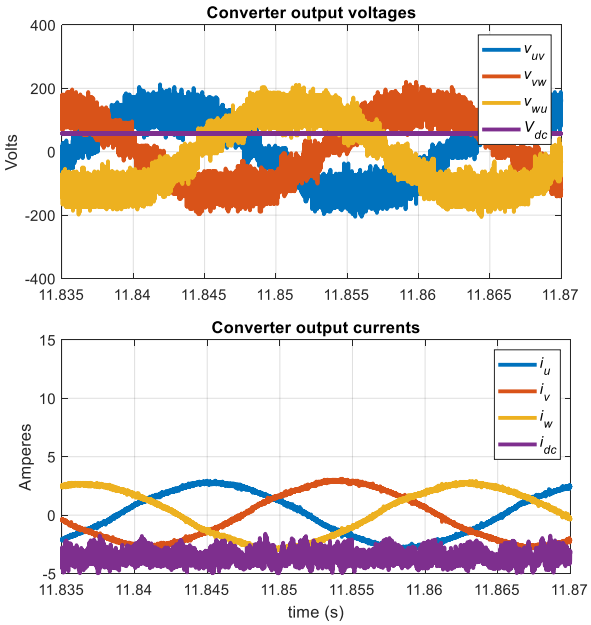

Fig. 13. Braking operations of the prototype BMCI.

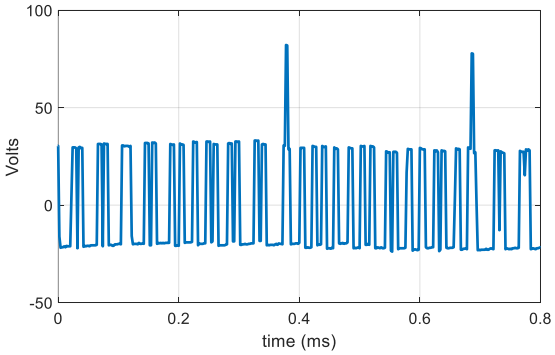

Fig. 14. Inductor voltage showing pulse coincidence due to aligned local duty-cycles of converter's arms.

waveforms align and causes an increment of the peak current ripple and an extra switching event.

VIII. Conclusion

This paper has presented a new type of boost voltage source inverter – the boost multilevel cascade inverter. The converter operations have been explained and examined in detail, presenting the model for the analysis of large and small-signal dynamics. The simulations for a light rail vehicle demonstrate the advantage of the proposed converter for fuel cells traction systems, as it compensates for the voltage regulation effect by changing the dc component of the modulation index. The design for a typical light train has shown that the weight and volume of passive components is significantly reduced compared to a standard boost inverter, therefore improving a key requirement for traction systems. The proposed converter is an excellent option to boost the voltage also when other primary sources like batteries are used. The efficiency curve of boost multilevel cascade inverters is higher at partial loads but lower at full load, albeit this is compensated by the higher efficiency of the motor as the current has a lower distortion. The proposed concept has been experimentally validated with a laboratory prototype. The experimental tests have proved that the proposed converter achieves high boost ratio with small inductors, while producing output voltage waveforms with low harmonic distortion. It has been finally shown experimentally that the proposed converter keeps the capacitor voltage ripple and the peak arm current within the design limits for the full speed range of the motor, including operations at low machine speed and high torque typically required by traction inverters.

References

[1] D. Furquim Pereira, F. da Costa Lopes, and E. H. Watanabe, "Nonlinear model predictive control for the energy management of fuel cell hybrid electric vehicles in real time", *IEEE Trans. Ind. Electron.*, vol. 68, no. 4, pp.3212 3223, Apr. 2021.

[2] Xiaogang Wu, Mingliang Yang, Meilan Zhou, Yu Zhang, and Jun Fu, "A novel high-gain dc-dc converter applied in fuel cell vehicles", *IEEE Trans. Veh. Technology*, vol. 69, no. 11, pp. 12763-12774, No. 2020.

[3] M. Sagar Bhaskar, V. K. Ramachandaramurthy, S. Padmanaban, F. Blaabjerg, D. M. Ionel, M. Mitolo, and D. Almakhles, "Survey of dc-dc non-isolated topologies for unidirectional power flow in fuel cell vehicles", *IEEE Access*, vol. 8, pp. 178130-178166, Oct. 2020.

[4] Guorui Zhang, Qi Li, Weirong Chen, and Xiang Meng, "Synthetic Strategy combining speed self-adjusting operation control and adaptive power allocation for fuel cell hybrid tramway", *IEEE Trans. Ind. Electron.*, vol. 68, no. 2, pp. 1454-1465, Feb. 2021.

[5] H. Moradisizkoohi, N. Elsayad, and O. A. Mohammed, "An integrated interleaved ultrahigh step-up dc–dc converter using dual cross-coupled inductors with built-in input current balancing for electric vehicles", *IEEE J. Emerging and Selected Topics in Power Electron.*, vol. 8, no. 1, pp. 644-657, Mar. 2020.

[6] W. Martinez, S. Kimura, J. Imaoka, M. Yamamoto, and C. A. Cortes, "Volume comparison of dc-dc converters for electric vehicles", in *Proc. of 2015 IEEE Workshop on Power Electron. and Power Quality Applications (PEPQA)*, pp. 1-6, 2015.

[7] R. Burkart and J. W. Kolar, "Component cost models for multi-objective optimizations of switched-mode power converters", in *Proc. of 2013 IEEE Energy Conversion Congress and Exposition*, pp. 2139-2146, 2013.

[8] Q. Lei and F. Z. Peng, "Space vector pulsewidth amplitude modulation for a buck-boost voltage/current source inverter", *IEEE Trans. Power Electron.*, vol. 29, pp. 266-274, Jan. 2014.

[9] Y. Liu and F. Z. Peng, "Fast control of PWAM boost-converter-inverter system for HEV/EV motor drives", in *Proc. of 2014 IEEE Appl. Power Electron. Conf. and Exposition APEC 2014*, pp. 2446-2452, 2014.

[10] R. Mayer, M. Berrehil El Kattel, and S. Vidal Garcia Oliveira, "Multiphase interleaved bidirectional dc/dc converter with coupled inductor for electrified-vehicle applications", *IEEE Trans. Power Electron.*, vol. 36, no. 3, pp. 2533-2547, Mar. 2021.

[11] J. Guo, R. Rodriguez, J. Gareau, D. Schumacher, M. Alizadeh, P. Azer, J. Bauman, B. Bilgin, and A. Emadi, "A comprehensive analysis for high-power density, high-efficiency 60 kW interleaved boost converter design for electrified powertrains", *IEEE Trans. Veh. Technology*, vol. 69, no. 7, pp. 7131-7145, Jul. 2020.

[12] S. Kimura, Y. Itoh, W. Martinez, M. Yamamoto, and J. Imaoka, "Downsizing effects of integrated magnetic components in high power density dc-dc converters for EV and HEV applications", *IEEE Trans. Ind. Appl.*, vol. 52, pp. 3294-3305, Jul./Aug. 2016.

[13] K. Yamanaka, H. Hara, T. Kume, and S. Ishii, "Bidirectional DC-AC current source inverter using coupled inductor", in *Proc. of 2012 IEEE 13th Workshop on Control and Modeling for Power Electron.*, pp. 1-6, 2012.

[14] D. Mande, J. P. Trovao, R. Gonzalez Rubio, and M. C. Ta, "Comparison of different power train topologies for an off-road electric vehicle", in *Proc. of 2019 IEEE Vehicle Power and Propulsion Conf.*, pp. 1 6, 2019.

[15] F. E. Alfaris and S. Bhattacharya, "A current-fed quasi Z-source inverter with SiC power modules for EV/HEV applications", in *Proc. of 2017 IEEE Energy Conversion Congress and Exposition*, pp. 5445-5452, 2017.

[16] S. Yang, F. Z. Peng, Q. Lei, R. Inoshita, and Z. Qian, "Current-fed quasi-Z-source inverter with voltage buck-boost and regeneration capability", *IEEE Trans. Ind. Appl.*, vol. 47, pp. 882-892, Mar./Apr. 2011.

[17] H. Chen, H. Kim, R. Erickson, and D. Maksimović, "Electrified automotive powertrain architecture using composite dc-dc converters", *IEEE Trans. Power Electron.*, vol. 32, pp. 98-116, 2017.

[18] D. Ronanki and S. S. Williamson, "A simplified space vector pulse width modulation implementation in modular multilevel converters for electric ship propulsion systems", *IEEE Trans. Transportation Electrification*, vol. 5, no. 1, pp. 335-342, Mar. 2019.

[19] A. Antonopoulos, L, Angquist, S. Norrga, K. Ilves, L. Harnefors, and H. P. Nee, "Modular multilevel converter ac motor drives with constant torque from zero to nominal speed", *IEEE Trans. Ind. Appl.*, vol. 50, pp. 1982-1993, 2014.

[20] D. De Simone, P. Tricoli, S. D'Arco, and L. Piegari, "Windowed PWM: a configurable modulation scheme for modular multilevel converter-based traction drives", *IEEE Trans. Power Electron.*, vol. 35, no. 9, pp. 9727-9736, Sep. 2020.

[21] L. He, K. Zhang, J. Xiong, S. Fan, and Y. Xue, "Low-Frequency ripple suppression for medium-voltage drives using modular multilevel converter with full-bridge submodules", *IEEE J. Emerging and Selected Topics in Power Electron.*, vol. 4, no. 2, pp. 657-667, Jun. 2016.

[22] L. He, K. Zhang, J. Xiong, S. Fan, and Y. Xue, "Low-Frequency ripple suppression for medium-voltage drives using modular multilevel converter with full-bridge submodules", *IEEE J. Emerging and Selected Topics in Power Electron.*, vol. 4, no. 2, pp. 657-667, Jun. 2016.

[23] Y. Rongfeng, W. Qiannan, C. Cecati, S. Xunwen, and X. Dianguo, "Asymmetric control with hybrid/full bridge modular multilevel converter for low frequency low voltage drive application" in *Proc. of IECON 2016 - 42nd Annual Conf. of IEEE Ind. Electron. Soc.*, pp. 6465-6469, 2016.

[24] J. Reed, G. Venkataramanan, D. Ramirez, and C. Soriano, "Design considerations for a voltage-boosting dc-ac modular multilevel

converter", in *Proc. of Applied Power Electron. Conf. and Exposition*, pp. 841-848, 2015.
[25] Y. Kumar and G. Poddar, "Control of Medium voltage ac motor drive for wide speed range using modular multilevel converter", *IEEE Trans. Ind. Electron.*, vol. 64, no. 4, pp. 2742-2749, Apr. 2017.
[26] M. Quraan, T. Yeo, and P. Tricoli, "Design and control of modular multilevel converters for battery electric vehicles", *IEEE Trans. Power Electron.*, vol. 31, pp. 507-517, 2016.
[27] J. Kim, J. Lee, and B. H. Cho, "Equivalent circuit modeling of PEM fuel cell degradation combined with a LFRC", *IEEE Trans. Ind. Electron.*, vol. 60, no. 11, pp. 5086-5094, Nov. 2013.
[28] Y. Tang, L. Ran, O. Alatise, and P. Mawby, "Capacitor selection for modular multilevel converter", *IEEE Trans. on Ind. Appl.*, vol. 52, no. 4, pp. 3279-3293, Jul./Aug. 2016.

Ivan Krastev was born on December 28, 1988 in Varna, Bulgaria. He received the M.Eng. degree and the Ph.D. degree in electronic and electrical engineering from the University of Birmingham, Birmingham, U.K., in 2012 and 2018, respectively.
Between 2014 and 2017 he led a team that designed and built a 10.25" gauge fuel cell locomotive for the Birmingham Centre for Railway Research and Education of the University of Birmingham. From 2017 to 2019 he worked at TMD technologies and specialised in high-voltage power supplies for travelling-wave tube amplifiers. He currently works as HTS Power Electronics Engineer at Tokamak Energy, Oxfordshire, U.K., developing power supplies and protection systems for hight-temperature superconducting magnets. His research interests include power converters for magnetic confinement fusion, renewable energy, and electric traction.

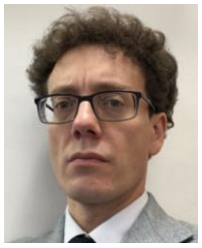

Pietro Tricoli (Member, IEEE) was born in Naples, Italy, on September 8, 1978. He received the M.S. (cum laude) and Ph.D. degrees in electrical engineering from the University of Naples Federico II, Naples, Italy, in 2002 and 2005, respectively.

He was a Visiting Scholar with the Department of Electrical and Computer Engineering, University of Wisconsin-Madison, Madison, WI, USA, in 2005. In 2006, he was also a Visiting Scholar with the Department of Electrical and Electronic Engineering, Nagasaki University, Nagasaki, Japan. From 2006 to 2011, he was a Postdoctoral Research Fellow with the Department of Electrical Engineering, University of Naples Federico II. In 2011 he moved to the Department of Electronic, Electrical, and Systems Engineering, University of Birmingham, Birmingham, U.K., as a Lecturer. He was promoted to Senior Lecturer in 2017 and to Reader in Power Electronics Systems in 2021. He is the author of more than 100 scientific papers published in international journals and conference proceedings. His research interests include storage devices for road electric vehicles, railways, and rapid transit systems, wind and photovoltaic generation, railway electrification systems and modeling and control of multilevel converters.

Dr. Tricoli is a member of the IEEE Industrial Electronics Society and the Energy Institute. He is the Web and Publication Chair of the International Conference on Clean Electrical Power. He is the Deputy Editor-in-Chief and Feature Editor of the IET Journal Renewable Power Generation. He is a Registered Professional Engineer in Italy.